Aalborg Universitet

AALBORG UNIVERSITY
DENMARK

Passivity-Based Design of Repetitive Controller for LCL-Type Grid-Connected Inverters Suitable for Microgrid Applications

Xie, Chuan; Liu, Dong; Li, Kai; Zou, Jianxiao; Zhou, Keliang; M. Guerrero, Josep

Published in:
IEEE Transactions on Power Electronics

DOI (link to publication from Publisher):
10.1109/TPEL.2020.3014365

Publication date:
2021

Document Version
Accepted author manuscript, peer reviewed version

Link to publication from Aalborg University

Citation for published version (APA):
Xie, C., Liu, D., Li, K., Zou, J., Zhou, K., & M. Guerrero, J. (2021). Passivity-Based Design of Repetitive Controller for LCL-Type Grid-Connected Inverters Suitable for Microgrid Applications. *IEEE Transactions on Power Electronics* , *36*(2), 2420-2431. [9159942]. https://doi.org/10.1109/TPEL.2020.3014365

General rights
Copyright and moral rights for the publications made accessible in the public portal are retained by the authors and/or other copyright owners and it is a condition of accessing publications that users recognise and abide by the legal requirements associated with these rights.

- Users may download and print one copy of any publication from the public portal for the purpose of private study or research.
- You may not further distribute the material or use it for any profit-making activity or commercial gain
- You may freely distribute the URL identifying the publication in the public portal -

Take down policy
If you believe that this document breaches copyright please contact us at vbn@aub.aau.dk providing details, and we will remove access to the work immediately and investigate your claim.

This article has been accepted for publication in a future issue of this journal, but has not been fully edited. Content may change prior to final publication. Citation information: DOI 10.1109/TPEL.2020.3014365, IEEE Transactions on Power Electronics

Passivity-Based Design of Repetitive Controller for LCL-Type Grid-Connected Inverters Suitable for Microgrid Applications

Chuan Xie, *Senior Member, IEEE*, Dong Liu, *Senior Member, IEEE*, Kai Li, *Member, IEEE*, Jianxiao Zou, *Member, IEEE*, Keliang Zhou, *Senior Member, IEEE* and Josep M. Guerrero, *Fellow, IEEE*

***Abstract*—Repetitive controller (RC) is one of the most promising candidates for harmonic compensation when designing the current controller of grid-connected inverters. The discrete-time closed-loop transfer function based frequency response method can be used to shape RC, which is applicable for a single inverter connecting to well-known inductive-impedance grids but cannot guarantee the stability in the case of capacitive-impedance grids or complex systems, such as microgrid. To address this issue, this paper presents a new passivity-based design method for RC for *LCL*-type grid-connected inverters with either inverter-side or grid-side current control. With the proposed design guidelines, the output admittance of the RC controlled inverter is tuned to be passive in all frequencies, so that it can be "plug and play" connected to a grid regardless of grid impedance. Meanwhile, thanks to infinite gains of RC at the fundamental frequency and its multiples, the high-quality grid injected current in accordance with IEC 61000-3-4 standard is ensured even in the presence of distorted grid conditions. Finally, experimental results with an established lab prototype are provided to verify the effectiveness of the proposed approach.**

***Index Terms*—Inverter control, repetitive control, *LCL*-filter, passivity, stability**

I. Introduction

With the development of highly penetrated renewable energy generation systems, more and more power inverters are employed to interface renewable energy generators to the grid [1]. Therefore, the quality of the grid injected current is getting special attention. To prevent a strong distortion of the grid voltage, the regulation IEC 61000-3-4 enforces a limit on the harmonics of the current fed into the grid. According to this regulation, a total harmonic distortion (THD) of 5% must not be exceeded [2]. Grid voltage harmonics can excite harmonics in the inverter current. These current harmonics vice versa can further excite voltage harmonics, resulting in a growing grid distortion as more inverter systems are connected to the grid. This effect is particularly strong in a weak grid. Thus, the controller of the inverter needs to reject voltage harmonics to prevent the excitation of higher order current harmonics.

The most popular current control method for grid-connected inverters are proportional-integral (PI) control [3], [4] and proportional-resonant (PR) control [5], [6]. The PI control method is usually used in the synchronous reference frame (SRF) and performs well under balanced systems. However, it is not suitable for the unbalanced system, which is common in the distributed power grid. The PR control method is widely used in the stationary frame since it is capable of tracking sinusoidal references of arbitrary frequencies at both positive and negative sequences with zero steady-state error [5], [6]. However, multiple paralleled resonators are needed to compensate dominant harmonics, and would thus increase the design complexity and computation burden [7]. In contrast, the repetitive controller (RC), which is originated from the internal model principle, can exactly track periodic reference signals and eliminate periodic disturbances with zero steady-state error [8], and has a relatively simple structure and small computation burden. In practical, RC has been widely applied to different power converter applications, e.g., active power filters (APFs) [9]–[11], uninterrupted power supplies (UPSs) [12]–[16], and grid-connected inverters [17]–[19], etc. As known, RC suffers from the sluggish dynamic response of one fundamental period delay and the performance degradation in the presence of grid frequency variation. To ease these drawbacks, parallel structure RC [20], fractional-order RC [17], and their combinations [21] are presented, respectively.

Although many achievements have been made in RC design and its applications, contributions are mainly focused on the modifications of the internal model. In previous works, the current design guidelines are almost on the basis of the frequency response of the closed-loop transfer function [8]–[21], which is only applicable for the internal stability analysis of individual inverter connecting to a well-known inductive grid. However, it's not applicable for the external stability analysis of inverters operating in a capacitive grid or a complex system like microgrid that comprises multiple inverters [22], [23]. In this paper, the internal stability refers to the stability of the current control closed-loop of the inverter with an ideal zero impedance grid [23], while the external stability refers to the

Manuscript received November 20, 2019; revised February 28 and June 10, 2020; accepted August 2, 2020. This work was supported by the National Natural Science Foundation of China under Grant No. 51807021 and 51707030, Sichuan Science and Technology Program under Grant No.2018HH0149 and the VILLUM FONDEN under the VILLUM Investigator Grant (no. 25920): Center for Research on Microgrids (CROM). (*Corresponding author: Chuan Xie, Dong Liu*)

C. Xie, K. Li and J. Zou are with the School of Automation Engineering, University of Electronic Science and Technology of China, Chengdu 611731, China (e-mail: c.xie@uestc.edu.cn; autolikai@gmail.com; jxzou@uestc.edu.cn).

D. Liu and J. M. Guerrero are with the Department of Energy Technology, Aalborg University, Aalborg 9220, Denmark (e-mail: dli@et.aau.dk; joz@et.aau.dk).

K. Zhou is with the School of Engineering, University of Glasgow, Glasgow G12 8QQ, United Kingdom (e-mail: Keliang.Zhou@glasgow.ac.uk)

0885-8993 (c) 2020 IEEE. Personal use is permitted, but republication/redistribution requires IEEE permission. See http://www.ieee.org/publications_standards/publications/rights/index.html for more information.
Authorized licensed use limited to: Aalborg Universitetsbibliotek. Downloaded on August 17,2020 at 06:26:16 UTC from IEEE Xplore. Restrictions apply.

This article has been accepted for publication in a future issue of this journal, but has not been fully edited. Content may change prior to final publication. Citation information: DOI 10.1109/TPEL.2020.3014365, IEEE Transactions on Power Electronics

stability of interactions between the inverter and the grid [24].

The external stability of the inverter can be assessed with the utilization of the impedance-based stability analysis method, which is originally presented to analyze the stability of DC systems [25], and then introduced to the investigation of AC system [26]. In the impedance-based stability analysis method, the external stability is determined by the impedance ratio seen at any given interface. In addition, stability margins can also be formulated by defining forbidden regions for the locus of the impedance ratio [27], or alternatively transformed into inverter output impedance specifications using Bode plots [28]. However, there is still lack of an impedance specification that ensures the stability of inverters to be immune to the changes in grid conditions. For improving the system stability robustness, the frequency domain passivity theory was introduced for grid-connected converters [29]. According to the passivity theory, the inverter will not destabilize the system if its output admittance is passive, i.e., 1) the inverter is internally stable and 2) the real part of the admittance is non-negative. If the grid impedance is also passive, then the whole grid-connected inverter system will be passive and stable. Intensive research have been carried out to deal with the passivity enhancement of grid-connected inverters with either inverter-side current control [24], [30] or grid-side current control [23], [31], [32]. Most recently, we have proposed a simple subadmittance combination method, which has unified the realization of all frequencies' passive output admittance for both inverter-side and grid-side current control [33]. However, literature concerning the passivity enhancement of inverter output admittance seldom consider harmonic control issues, and PR controllers are commonly used [23], [31]–[33]. The effect of multiple resonant controllers on the passivity of the inverter has been investigated in [34], and design guidelines are also developed to avoid non-passive admittance about the resonator frequencies. To the best knowledge of the authors, how to develop design guidelines for RCs to ensure the passive behavior of the inverter output impedance is still a white spot.

In light of this, this paper presents an original passivity-based design method for RCs for LCL-type grid-connected inverters with either inverter-side or grid-side current control. The rest of the paper is organized as follows: The system configuration of studied three-phase LCL-type grid-connected inverter and its corresponding admittance model for controller parameter design are introduced in Section II. Then, in Section III, a unified passivity-based controller design guidelines applicable for either inverter-side or grid-side current-controlled inverter is proposed, whereby passive output admittance of the inverter in all frequencies is obtained. Simulation and Experimental results are provided in Section IV to verify the theoretical analysis and Section V summarizes the paper.

II. System Configuration and Modeling of the LCL-Type Grid-Connected Inverter

A. System Description and Modeling

Fig. 1 shows the system configuration of the studied three-phase LCL-type grid-connected voltage-source inverter (VSI). In Fig. 1, L_1, L_2, C represent the inverter-side inductor, grid-side inductor, and capacitor of the LCL-filter, L_g is the grid

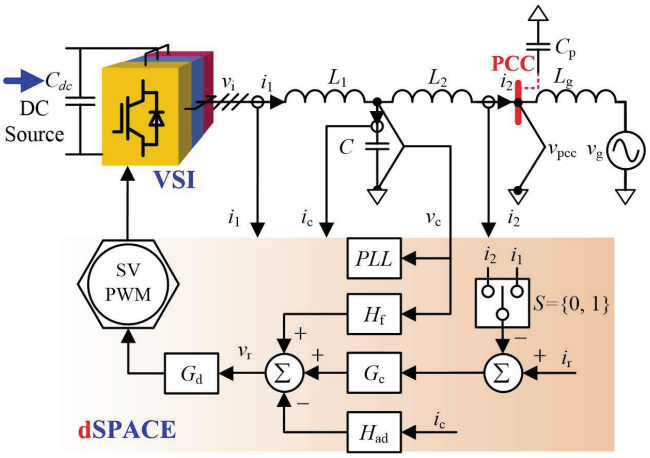

Fig. 1. System configuration of the studied three-phase LCL-type grid-connected inverter.

leakage inductor, C_p is the power factor correction (PFC) capacitor connected at point of common coupling (PCC). The parasitic resistances of all inductors are neglected for the worst case with zero passive damping. In the same figure, $i_1, i_2, i_c, v_i, v_c, v_{pcc}$ and v_g represent the inverter-side current, grid-side current, capacitor current, inverter output voltage, capacitor voltage, voltage of PCC and grid voltage; and G_c, H_{ad}, H_f and G_d represent current controller, capacitor current feedback active damping (CCF-AD) controller and capacitor voltage feedforward active damping (CVF-AD) controller and system delays (including sampling and pulse width modulation (PWM)), respectively.

With the symbols as defined in Fig. 1, the dynamic equations of the LCL-filtered grid-connected inverter can be expressed as follows [35].

$$\begin{cases} L_1 \frac{di_1}{dt} = v_i - v_c \\ L_2 \frac{di_2}{dt} = v_c - v_{pcc} \\ i_1 = i_c + i_2 \\ C \frac{dv_c}{dt} = i_c \end{cases} \tag{1}$$

Applying the *Laplace* transformation to (1), the corresponding s-domain equations can be obtained as (2),

$$\begin{cases} L_1 s \cdot I_1(s) = V_i(s) - V_c(s) \\ L_2 s \cdot I_2(s) = V_c(s) - V_{pcc}(s) \\ I_1(s) = I_c(s) + I_2(s) \\ Cs \cdot V_c(s) = I_c(s) \end{cases} \tag{2}$$

where the uppercase symbols represent the corresponding s-domain variables.

B. Control Scheme

As shown in Fig. 1, both i_1 and i_2 are fed back as control objectives and selected by a switch, S, before feeding to the current controller $G_c(s)$, the detailed structure of which is shown in Fig. 3. Note that S = 1 represents the inverter-side current control works, while S = 0 represents the grid-side current control works. For the objective of active damping, both feedback of the capacitor current through $H_{ad}(s)$ and feedforward of the capacitor voltage through $H_f(s)$ are also

0885-8993 (c) 2020 IEEE. Personal use is permitted, but republication/redistribution requires IEEE permission. See http://www.ieee.org/publications_standards/publications/rights/index.html for more information.
Authorized licensed use limited to: Aalborg Universitetsbibliotek. Downloaded on August 17,2020 at 06:26:16 UTC from IEEE Xplore. Restrictions apply.

This article has been accepted for publication in a future issue of this journal, but has not been fully edited. Content may change prior to final publication. Citation information: DOI 10.1109/TPEL.2020.3014365, IEEE Transactions on Power Electronics

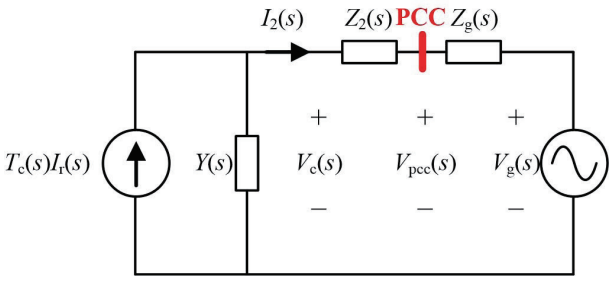

Fig. 2. Equivalent circuit for the grid-connected inverter.

included in the control law, to give the following inverter-voltage reference [33]:

$$V_r(s) = \{I_r(s) - [S \cdot I_1(s) + (1-S) \cdot I_2(s)]\} G_c(s) - H_{ad}(s) I_c(s) + H_f(s) V_c(s) \tag{3}$$

where I_r is the current reference.

The inverter output voltage v_i is created by PWM. The DC-link voltage is regarded as constant for simplicity and bandwidth of the phase-locked loop (PLL) is designed smaller than the grid fundamental frequency to avoid unintentional low-frequency interaction [24]. Taking the typical delay of $1.5T_s$ into consideration, the inverter output voltage can be expressed as.

$$V_i(s) = V_r(s) G_d(s) \tag{4}$$

where $G_d(s) = e^{-T_d s}$ and $T_d = 1.5T_s$.

C. General Admittance Model

Substituting (3) and (4) into (2), with i_2 and v_c regarded as the output and disturbance, respectively, giving

$$I_2(s) = T_c(s) I_r(s) - Y(s) V_c(s) \tag{5}$$

where the inner closed-loop system ($T_c(s)$) and the inner total output admittance ($Y(s)$), respectively, are given by

$$T_c(s) = \frac{G_c(s) G_d(s)}{L_1 s + G_c(s) G_d(s)} \tag{6}$$

and

$$Y(s) = \frac{1 + L_1 C s^2 + \{[S \cdot G_c(s) + H_{ad}(s)] \cdot Cs - H_f(s)\} G_d(s)}{L_1 s + G_c(s) G_d(s)} \tag{7}$$

Based on (7), the equivalent circuit can be obtained as shown in Fig. 2, in which $Z_2(s) = L_2 s$ and $Z_g(s)$ is the grid impedance.

III. Passivity-Based Controller Parameters Design

A. Overall Closed-Loop System Stability Condition

According to in Fig. 2, combining (5) with the equation that $V_c(s) = V_g(s) + I_2(s)[Z_2(s) + Z_g(s)]$, the overall closed-loop current response seen from the v_g, which is the stiff grid voltage behind the grid impedance, can be derived as

$$I_2(s) = \frac{T_c(s)}{1 + [Z_2(s) + Z_g(s)] Y(s)} I_r(s) - \frac{Y(s)}{1 + [Z_2(s) + Z_g(s)] Y(s)} V_g(s) \tag{8}$$

From (8), the overall closed-loop system is stable if the following two conditions hold [29], [30].

1) The inner closed-loop system ($T_c(s)$) is asymptotic stable.
2) The roots of $1 + [Z_2(s) + Z_g(s)] Y(s) = 0$ are all located in the left half of the s-plane.

In the derived system model, both inverter-side and grid-side current control have an identical inner closed-loop system, as expressed in (6), which is a first-order system with a pure delay element and can thus be easily stabilized by introducing indexes of the open-loop system's gain crossover frequency and the associated phase margin (PM) [33]. Then, the second stability condition (external stability) can be analyzed by applying the Nyquist criterion to the open-loop transfer function $[Z_2(s) + Z_g(s)] Y(s)$, i.e., impedance ratio between grid and inverter [26]. However, a more conservative stability constraint is that both $[Z_2(s) + Z_g(s)]$ and $Y(s)$ are passive [30]. As long as $[Z_2(s) + Z_g(s)]$ represents a resistive-inductive-capacitive (RLC) network, it is obviously passive. Remaining is to make $Y(s)$ passive.

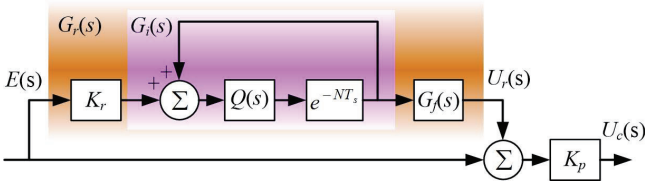

Fig. 3. Block diagram of the "plug-in" repetitive controller [9].

B. Preliminary Parameters Selection for the Inner Stability

Regardless of the passivity constraints of the inverter output admittance, the controller parameters can be preliminarily selected via the transfer function-based frequency response method. Although this has been already well discussed in many papers [8], [9], [13], it's re-introduced briefly in this paper.

The detailed block diagram of the used "plug-in" repetitive controller is depicted in Fig. 3. According to Fig. 3, the current controller can be expressed as

$$G_c(s) = \frac{U_c(s)}{E(s)} = K_p[1 + G_r(s)] \tag{9}$$

where K_p is the proportional gain, $G_r(s)$ is the RC with the following expression.

$$G_r(s) = \frac{U_r(s)}{E(s)} = K_r G_i(s) G_f(s) = K_r \frac{Q(s) e^{-NT_s s}}{1 - Q(s) e^{-NT_s s}} G_f(s) \tag{10}$$

0885-8993 (c) 2020 IEEE. Personal use is permitted, but republication/redistribution requires IEEE permission. See http://www.ieee.org/publications_standards/publications/rights/index.html for more information.
Authorized licensed use limited to: Aalborg Universitetsbibliotek. Downloaded on August 17,2020 at 06:26:16 UTC from IEEE Xplore. Restrictions apply.

This article has been accepted for publication in a future issue of this journal, but has not been fully edited. Content may change prior to final publication. Citation information: DOI 10.1109/TPEL.2020.3014365, IEEE Transactions on Power Electronics

where K_r is the RC gain, T_s is the control period, N is the ratio of the sampling frequency and fundamental frequency of the grid. $G_f(s)$ is the compensator which could be a pure leading element [13], i.e., $G_f(s) = e^{mT_s s}$, and $Q(s) = a_1 e^{T_s s} + a_0 + a_1 e^{-T_s s}$ with $2a_1 + a_0 = 1$ is a low-pass filter (LPF) to improve the robustness of the system [10].

*1) **Selection of the Proportional Gain** K_p:* Assuming K_r = 0, the proportional gain K_p can be firstly designed according to the open-loop transfer function of the inner closed-loop system with only proportional control.

$$T_{op}(s) = K_p G_d(s)/L_1 s \tag{11}$$

The phase angle of the above open-loop transfer function at the crossover angular frequency ω_c is given by

$$\begin{aligned}\angle T_{op}(j\omega_c) &= \angle\{K_p G_d(j\omega_c)\frac{1}{sL_1}\} = \angle\{K_p e^{-j\omega_c T_d}\frac{1}{j\omega_c L_1}\} \\ &= -\omega_c T_d - \frac{\pi}{2} = -\pi + \varphi_m \end{aligned}\tag{12}$$

where φ_m is the desired phase margin (PM). The crossover frequency ω_c can be rewritten as

$$\omega_c = \frac{\pi/2 - \varphi_m}{T_d} \tag{13}$$

For a given φ_m, the proportional gain K_p can be obtained as (14) by setting the open-loop gain at the value of ω_c to unity using (11).

$$K_p = \omega_c L_1 \tag{14}$$

*2) **Selection of m and** K_r **for RC**:* Substituting $(9)-(11)$ into (6), the inner closed-loop system transfer function can be rewritten as

$$T_c(s) = \frac{T_{cp}(s)\{1 - Q(s)e^{-NT_s s}[1 - K_r G_f(s)]\}}{1 - Q(s)e^{-NT_s s}[1 - K_r G_f(s) T_{cp}(s)]} \tag{15}$$

where $T_{cp}(s) = T_{op}(s)/[1 + T_{op}(s)]$ represents the inner closed-loop transfer function with only proportional control.

Since $T_{cp}(s)$ is asymptotically stable, $T_c(s)$ is stable if the following condition holds [8].

$$\|Q(s)[1 - K_r G_f(s) T_{cp}(s)]\| \le 1 \tag{16}$$

It is not easy to choose m and K_r for the RC since they are coupled in (16). Following the frequency-domain design approach in [13], $T_{cp}(s)$ can be expressed as $T_{cp}(j\omega) = N(\omega)e^{j\theta(\omega)}$, with $N(\omega)$ and $\theta(\omega)$ being its magnitude and phase characteristics, respectively. $G_f(s)$ and $Q(s)$ can be expressed as $G_f(j\omega) = e^{jm\omega T_s}$ and $Q(j\omega) = a_0 + 2a_1 cos(\omega T_s)$, respectively. Then, (16) can be rewritten as

$$\begin{aligned}\left\|1 - K_r N(\omega) e^{j[\theta(\omega) + m\omega T_s]}\right\| &\le \frac{1}{\|Q(j\omega)\|} \\ &= \frac{1}{a_0 + 2a_1 \cos(\omega T_s)}\end{aligned}\tag{17}$$

By using the Euler expansion, (17) can be further rewritten as

$$0 \le K_r \le f(m,\omega) = \frac{a(\omega) + \sqrt{b(\omega)}}{N(\omega)} \tag{18}$$

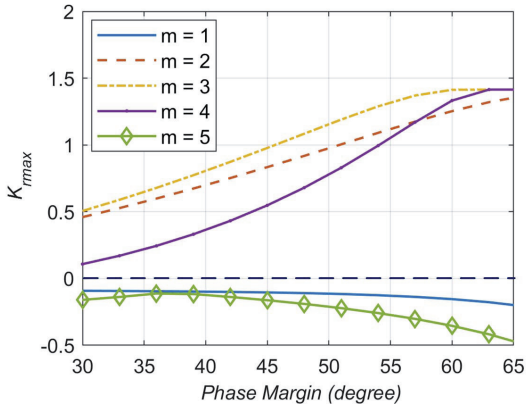

Fig. 4. Curves for K_{rmax} as a function of PM for different values of m (a_1 = 0.25 and a_0 = 0.5).

where

$$\begin{aligned}a(\omega) &= \cos[\theta(\omega) + m\omega T_s], \\ b(\omega) &= \frac{1}{[a_0 + 2a_1\cos(\omega T_s)]^2} - \sin^2[\theta(\omega) + m\omega T_s], \\ N(\omega) &= \omega_c/\sqrt{\omega^2 + \omega_c^2 - 2\omega\omega_c \sin(\omega T_d)}, \\ \theta(\omega) &= -\pi + \arctan\frac{\omega\cos(\omega T_d)}{\omega\sin(\omega T_d) - \omega_c}.\end{aligned}$$

Eq. (18) holds if K_r is smaller than the minima of $f(m,\omega)$, thus the upper boundary of K_r, i.e., K_{rmax}, is set to the minima of $f(m,\omega)$. For K_{rmax}, although it's difficult to get analytical results, the numerical results can be easily obtained by using the mathematic software, e.g., Matlab. Fig. 4 shows the curves for K_{rmax} as a function of PM for different values of m when a_1 = 0.5 and a_0 = 0.25. It can be seen from Fig. 4 that the value of m has a significant effect on the upper boundary of K_r, so an appropriate value should be selected. For the same m, a larger PM has a bigger K_{rmax}. It should be also noted that, according to (13), a larger PM has a smaller ω_c, viz., a relatively narrow inner closed-loop bandwidth.

C. Passivity-Based External Stability Check

*1) **Selection of Parameters for CCF-AD and CVF-AD**:* The external stability is guaranteed by making $Y(s)$ passive, viz., the real part of $Y(s)$ is non-negative. Without RC, all frequencies' non-negative real part of $Y(s)$ can be achieved via the combination of proportional CCF-AD, i.e., $H_a d(s)$ = K_{ad}, and CVF-AD. An analytical parameter design method for CCF-AD and CVF-AD to realize all frequencies' passive output admittance has been introduced in detail in [33], the results are directly cited hereinafter for the sake of the overall integrality and readability of this paper.

Feedback gains of CCF-AD for the inverter-side and grid-side current can be calculated using following two equations, accordingly.

$$K_{ad} = -\frac{36\omega_c}{C\omega_s^2} \tag{19}$$

0885-8993 (c) 2020 IEEE. Personal use is permitted, but republication/redistribution requires IEEE permission. See http://www.ieee.org/publications_standards/publications/rights/index.html for more information.
Authorized licensed use limited to: Aalborg Universitetsbibliotek. Downloaded on August 17,2020 at 06:26:16 UTC from IEEE Xplore. Restrictions apply.

This article has been accepted for publication in a future issue of this journal, but has not been fully edited. Content may change prior to final publication. Citation information: DOI 10.1109/TPEL.2020.3014365, IEEE Transactions on Power Electronics

and

$$K_{ad} = \omega_c L_1 - \frac{36\omega_c}{C\omega_s^2} \tag{20}$$

where ω_s is the sampling angular frequency that equals $2\pi/T_s$.

In practice, the CVF-AD controller $H_f(s)$ is consists of a bandpass filter (BPF) and a scaled first-order finite-impulse response low pass filter (FIR–LPF) as follows [33].

$$\begin{aligned} H_f(s) &= K_f G_{LPF}(s) + K_{fb} G_{BPF}(s) \\ &= K_f \overbrace{(1 - a + ae^{-sT_s})}^{G_{LPF}(s)} + K_{f\mathrm{b}} \overbrace{\omega_{bc} \frac{s\cos\phi_b - \omega_1 \sin\phi_b}{s^2 + \omega_{bc}s + \omega_1^2}}^{G_{BPF}(s)} \end{aligned} \tag{21}$$

where K_f and a are the feedforward gain of CVF-AD and parameter of FIR–LPF, respectively, both of them are constants less than one. K_{fb}, ω_1, ω_{bc} and ϕ_1 are the gain, fundamental angular frequency, cutoff angular frequency and compensation angle of the BPF, respectively. ω_{bc} is simply set to $0.1\omega_1$ to achieve a compromise between frequency selectivity and dynamic response. The time delay at the fundamental frequency is compensated by setting $H_f(j\omega_1) \approx e^{j\omega_1 T_d}$, which is achieved by letting

$$\varphi_b = \arctan \frac{\sin(\omega_1 T_d)}{\cos(\omega_1 T_d) - K_f} \tag{22}$$

and

$$K_{f\mathrm{b}} = \frac{\sin(\omega_1 T_d)}{\sin\phi_b} \approx 1 - K_f \tag{23}$$

*2) **Passivity Criteria for** m **and** K_r **Selection**:* When embedding RC into the control, the passivity of output admittance will degrade since the effect of infinite gain of RC, as shown in Figs. 5 and 6. The core parameters of RC, i.e., m and K_r, can be further refined from preliminary values to refined values for enhancing the passivity of output admittance and avoiding violation of first stability condition. Figs. 5 and 6 give curves for the real part of the output admittance of the inverter-side and grid-side current control for different values of m when K_r = 1.45. It is apparent that m = 2 is an optimal value for the inverter-side current controller, while m = 4 is more appropriate for the grid-side current control, to achieve a relatively better overall passivity of the output admittance.

Although the refined parameter m can improve the overall passivity of the output admittance, whereas the non-negative real part of output admittance may still exist. Considering that embedding RC will impair the overall passivity, thus reducing K_r to weaken the control effort of RC can undoubtedly enhance the overall passivity, and even realize all frequencies' passive output admittance, as shown in Fig. 7. However, it will also inevitably degrade the dynamic response speed of RC. Note that the obtained theoretical value for K_r may be a little pessimistic since no physical damping has been taken into consideration. A bigger value of K_r may be valid in the experiments.

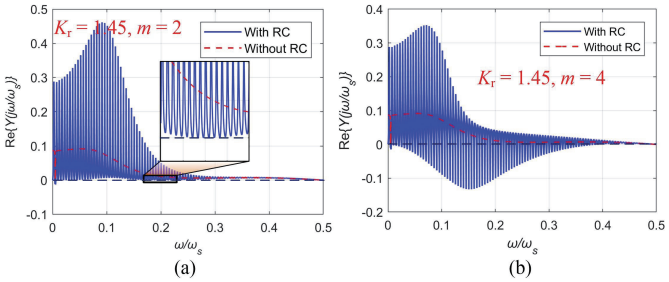

Fig. 5. Real part of the output admittance of the inverter-side current control with RC for different values of m when K_r = 1.45. (a) m = 2, (b) m = 4.

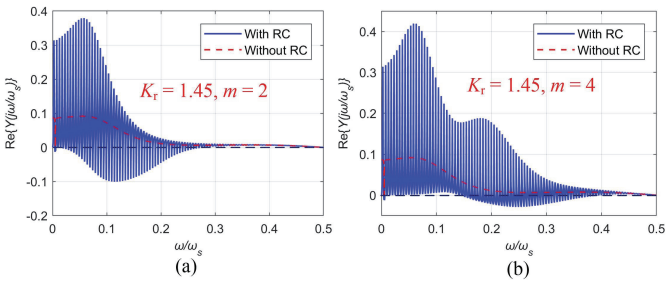

Fig. 6. Real part of the output admittance of the grid-side current control with RC for different values of m when K_r = 1.45. (a) m = 2, (b) m = 4.

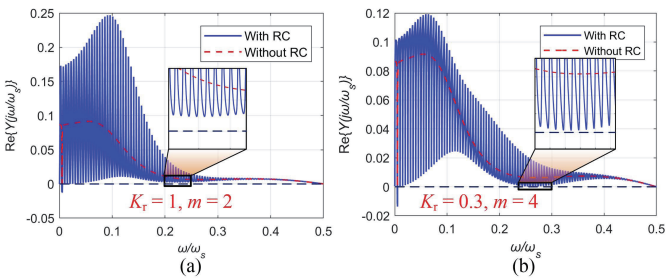

Fig. 7. Real part of the output admittance of either (a) inverter-side or (b) grid-side current control with reduced K_r.

IV. Simulation and Experimental Verifications

In order to verify the correctness of theoretical stability analysis and the effectiveness of the proposed controller parameter design method, a laboratory experimental setup is built up as shown in Fig. 8. The setup consists of four three-phase $Danfoss$ inverters with LCL filters, one of them is used for the following experiments. The designed control algorithm is implemented in a dSPACE 1005-based platform for real-time control. The power stage parameters are listed in Table I.

In this paper, the PM (φ_m) of the inner-loop is set to $\pi/3$ radians (60 degrees). Then, substituting the values of φ_m and T_d ($1.5/f_s$) into (13), ω_c can be obtained, i.e., ω_c = $0.056\omega_s$. Inverter-side and grid-side current control schemes share the same controller parameters for proportional gain and CVF-AD, which are directly calculated by using (14), (22) and (23). The parameters for CCF-AD are calculated by using (19) and (20). All results are listed in Table II. For RC, different RC gain K_r and lead step m are tested for both inverter-side current and grid-side current control in the experiments.

The inverter output admittance of both inverter-side and

0885-8993 (c) 2020 IEEE. Personal use is permitted, but republication/redistribution requires IEEE permission. See http://www.ieee.org/publications_standards/publications/rights/index.html for more information.
Authorized licensed use limited to: Aalborg Universitetsbibliotek. Downloaded on August 17,2020 at 06:26:16 UTC from IEEE Xplore. Restrictions apply.

This article has been accepted for publication in a future issue of this journal, but has not been fully edited. Content may change prior to final publication. Citation information: DOI 10.1109/TPEL.2020.3014365, IEEE Transactions on Power Electronics

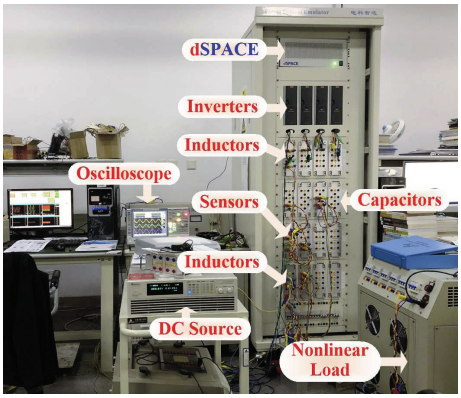

Fig. 8. Hardware picture for the experimental setup.

TABLE I
NOMINAL POWER STAGE PARAMETERS

	Symbol	Description	Value(p.u.)
Inverter	V_{dc}	Input DC voltage	350 V(1)
	S_N	Rated Power	1.4 kW(1)
	L_1	Inverter-side inductor	2.0 mH(0.024)
	C	Capacitor of LCL-filters	15 μF(8.19)
	L_2	Grid-side inductor	0.4 mH(0.005)
	f_s	Sampling and switching frequency	10 kHz(200)
	ω_s	Sampling angular frequency	62832 rad/s(200)
Grid	V_g	Grid voltage (Phase-to-ground RMS Voltage)	110 V(1)
	f_g	Frequency	50 Hz(1)
	L_g	Grid leakage inductors	0.2 mH, 9 mH (0.002, 0.11)
	C_p	PFC capacitor	22 μF(5.58)

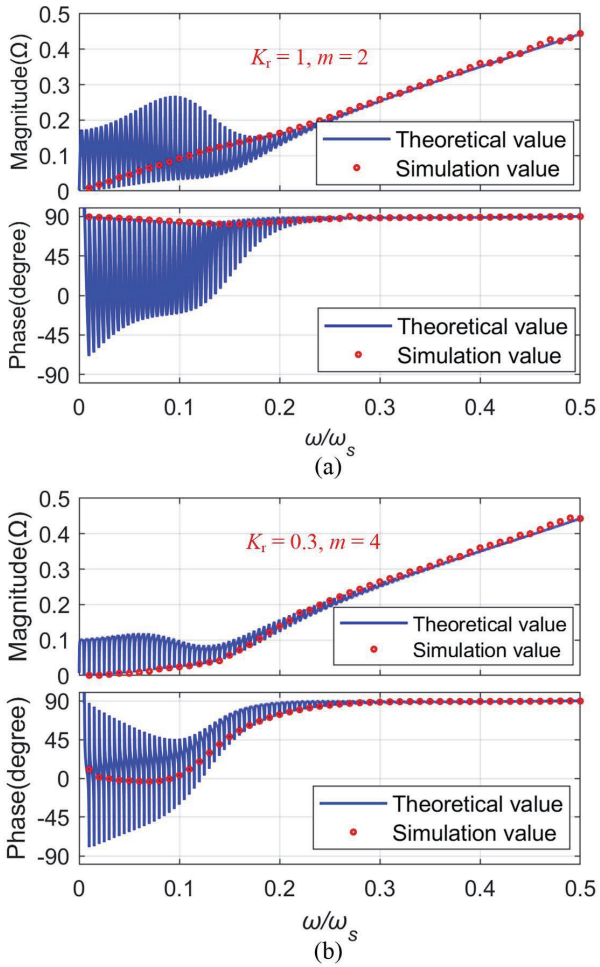

Fig. 9. Bodeplots of the inverter output admittance. (a) Inverter-side current control. (b) Grid-side current control.

grid-side current control are shown in Fig. 9. It should be mentioned that the results in Fig. 9 are obtained by simulation and the measurement procedure is similar to [31]. In the simulation, the voltage harmonics up to 100^{th} harmonic component (5 kHz) are applied at grid voltage (v_g), while the inverter reference current (i_r) is set to 0. Then, the fast Fourier transform of grid injected current (i_2) is calculated and subsequently the simulation results for $Y(s)(Y_{sim}(j\omega))$ can be achieved as follows:

$$Y_{sim}(j\omega) = \frac{|I_2(j\omega)|}{|V_c(j\omega)|} e^{\pi + \angle I_2(j\omega) - \angle V_c(j\omega)} \tag{24}$$

As shown in Fig. 9, $Y_{sim}(j\omega)$ well matches the theoretical expression given by (7). It can be also observed from Fig. 9 that grid-side current control has a better harmonic rejection ability over the inverter-side current control.

Both the inverter-side and grid-side current controllers of the inverter with RC are tested in different grid scenarios, viz., stiff inductive-impedance, weak inductive-impedance and capacitive-impedance grids. Before conducting experiments, theoretical stability assessments are performed by using Bode plots of both inverter output admittance and grid admittance. Normally, the stability, in terms of PM, can be interpreted by the phase difference at the intersection point of the magnitude responses of the inverter output admittance and grid admittance [23], [26], viz., the phase difference over 180 degrees indicates instability and vice versa. Since the passive output admittance in all frequencies is achieved with the proposed method, viz., the system stability is ensured regardless of the intersection locations of the magnitude responses of the inverter output admittance and grid admittance, only Bode plots for the inverter output admittance having non-passive

TABLE II
CONTROLLER PARAMETERS

	Symbol	Description	Value
Proportional Controller	K_p	Proportional gain	6.98 Ω
CCF-AD	K_{ad}	CCF gain for inverter-side current control	-2.12 Ω
	K_{ad}	CCF gain for grid-side current control)	4.86 Ω
CVF-AD	K_f	CVF gain	0.4 rad/s
	K_{fb}	BPF gain	0.6 rad/s^2
	a	Coefficient of FIR-LPF	0.5
	ω_{br}	Cut-off angular frequency	31.4 rad/s
	φ_b	Phase compensation angle	0.08 rad

0885-8993 (c) 2020 IEEE. Personal use is permitted, but republication/redistribution requires IEEE permission. See http://www.ieee.org/publications_standards/publications/rights/index.html for more information.
Authorized licensed use limited to: Aalborg Universitetsbibliotek. Downloaded on August 17,2020 at 06:26:16 UTC from IEEE Xplore. Restrictions apply.

This article has been accepted for publication in a future issue of this journal, but has not been fully edited. Content may change prior to final publication. Citation information: DOI 10.1109/TPEL.2020.3014365, IEEE Transactions on Power Electronics

regions are given to explicate the system instability condition. In addition, to unify and facilitate the stability assessments for different control objectives and scenarios, the inverter output admittance seen from PCC (see in Fig. 2) is thus redefined as $Y_{it}(s) = Y_i(s)/[Z_2(s)+Y_i(s)]$ (i = 1, 2. 1 stands for inverter-side current control, 2 stands for grid-side current control).

A. Tests in Stiff Inductive-Impedance Grid Scenario

The Bode plots of the inverter output admittance and grid admittance for L_g = 0.2 mH (0.002 p.u.) are shown in Fig. 10 when m = 4 and K_r = 1 for RC. As seen in Fig. 10, the inverter output admittance exactly intersects with grid admittance in the non-passive region (around 2 kHz), so the PM is negative and the system is unstable. The corresponding experimental waveforms of the inverter-side and grid-side current control are given in Figs. 11 and 12. These figures show, from top to bottom, the PCC voltage, the inverter-side current, the grid-side current and their corresponding frequency spectra, respectively.

As seen in Fig. 11 (a) and (b), when K_r = 1 and m changes from 2 to 4 for RC, viz., the inverter output admittance changes from all frequencies passive to partially non-passive and the output current of the inverter begins to oscillate gradually, which validates the theoretical expectations in Fig. 10 (a). Note that both the component at the intersection frequency, i.e., 2 kHz and the components below 2 kHz are amplified, which may be induced by the negative resistor effect of the inverter. Fig. 11 (c) gives dynamic experimental waveforms when K_r = 1 and m = 2 for RC, in which one fundamental period delay can be observed due to the inherent characteristic of RC, and the output current fully tracks the reference current within two fundamental periods.

Fig. 12 (a) and (b) show the experimental waveforms when m = 4 and K_r changes from 0.3 to 1 for RC, viz., the inverter output admittance changes from all frequencies passive to partially non-passive. From Fig. 12 (b), it can be observed that the output current of the inverter begins to oscillate and the system enters instability from stability, which validates the theoretical expectations in 10 (b). Different from the case of inverter-side current control, the oscillation component of grid-side current control is dominant around the intersection frequency, i.e., 2 kHz, the reason may be that the non-passive region of grid-side current control is only around 2 kHz as seen in Fig. 10 (b). Fig. 12 (c) gives dynamic experimental waveforms when K_r = 0.3 and m = 4 for RC, in which the dynamic response speed is obviously slower than that in Fig. 11 (c) due to the reduced RC gain.

B. Tests in Weak Inductive-Impedance Grid Scenario

The Bode plots of the inverter output admittance and grid admittance for L_g = 9 mH (0.11 p.u.) are shown in Fig. 13, when m = 4 and K_r = 1 for RC. As shown in Fig. 13 (a), the inverter output admittance of inverter-side current control intersects with grid admittance in the non-passive region, so the PM is negative and the system is unstable. In contrast, as shown in Fig. 13 (b), although the inverter output admittance of grid-side current control has non-passive

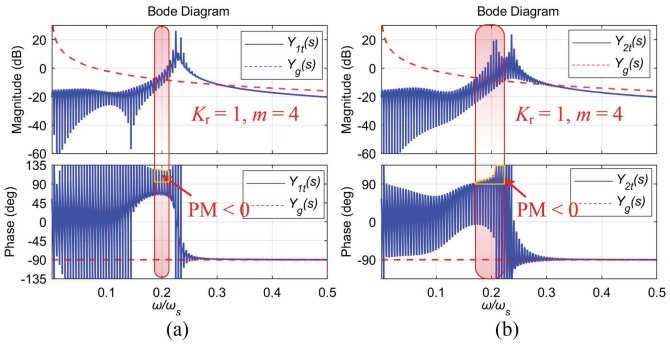

Fig. 10. Bode plots of $Y_{it}(s)$ and $Y_g(s)$ with m = 4 and K_r = 1 for RC and L_g = 0.2 mH(0.002 p.u.). (a) Inverter-side current control. (b) Grid-side current control.

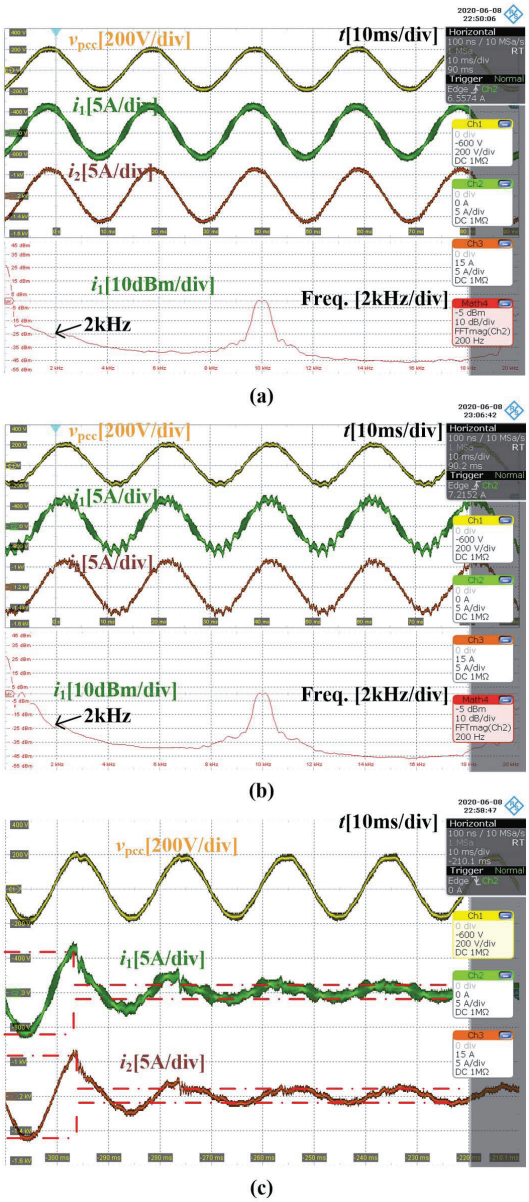

Fig. 11. Experimental waveforms of the inverter-side current control when K_r = 1 and m changes from (a) 2 to (b) 4. (c) Step change of reference current (6A to 1A, m = 2).

0885-8993 (c) 2020 IEEE. Personal use is permitted, but republication/redistribution requires IEEE permission. See http://www.ieee.org/publications_standards/publications/rights/index.html for more information.
Authorized licensed use limited to: Aalborg Universitetsbibliotek. Downloaded on August 17,2020 at 06:26:16 UTC from IEEE Xplore. Restrictions apply.

This article has been accepted for publication in a future issue of this journal, but has not been fully edited. Content may change prior to final publication. Citation information: DOI 10.1109/TPEL.2020.3014365, IEEE Transactions on Power Electronics

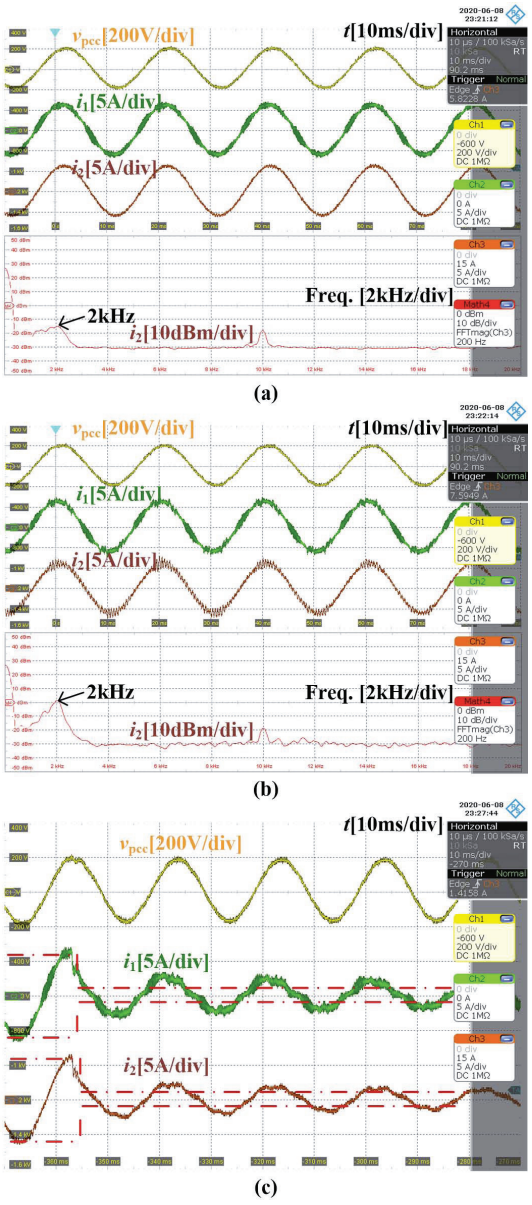

Fig. 12. Experimental waveforms of the grid-side current control when m = 4 and K_r changes from (a) 0.3 to (b) 1. (c) Step change of reference current (6A to 1A, K_r = 0.3).

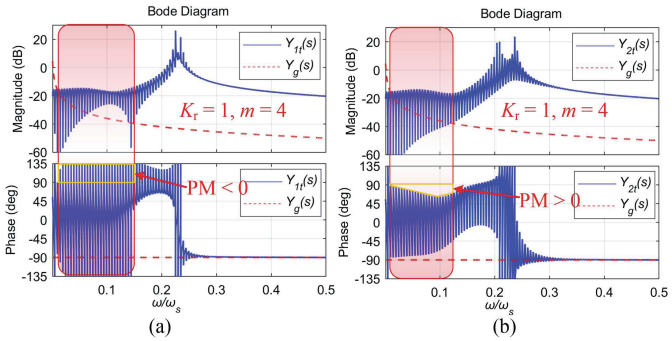

Fig. 13. Bode plots of $Y_{it}(s)$ and $Y_g(s)$ with m = 4 and K_r = 1 for RC and L_g = 9 mH (0.11 p.u.). (a) Inverter-side current control. (b) Grid-side current control.

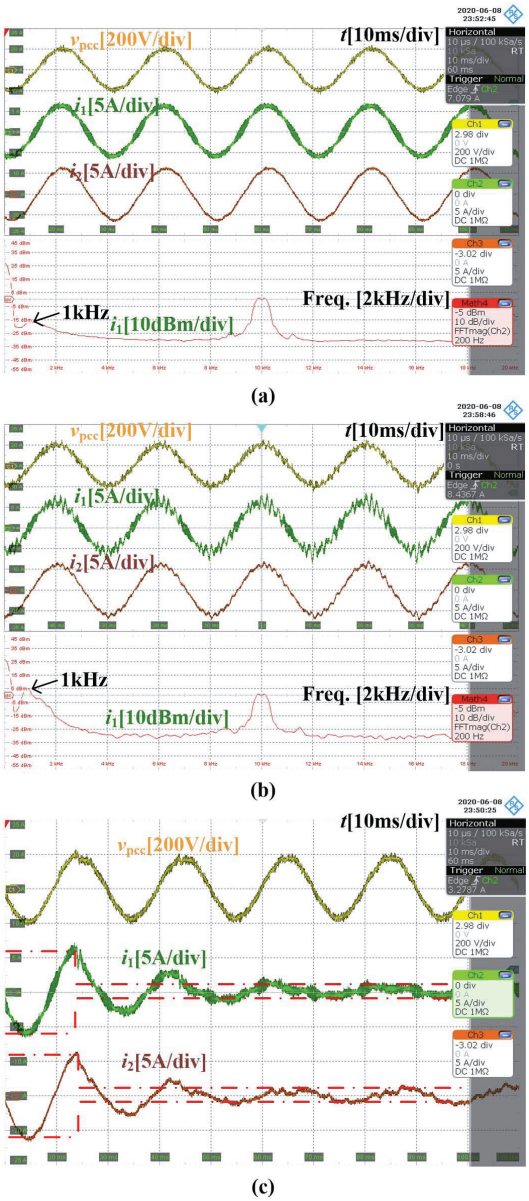

Fig. 14. Experimental waveforms of the inverter-side current control when K_r = 1 and m changes from (a) 2 to (b) 4. (c) Step change of reference current (6A to 1A, m = 2).

regions, it intersects with grid admittance in the passive region. Therefore, the PM is positive and the system is stable.

Fig. 14 (a) and (b) show the experimental waveforms when K_r = 1 and m changes from 2 to 4 for RC, viz., the inverter output admittance changes from all frequencies passive to partially non-passive, in which the output current begins to oscillate. The dominant oscillation component is at the intersection frequency, i.e., 1 kHz, as shown in Fig. 14 (b). Fig. 14 (c) gives dynamic experimental waveforms, in which the dynamic response speed is comparable with that in Fig. 11 (c). Fig. 15 only gives the dynamic experimental waveform of the step change of reference current for the grid-side current control when m = 4 and K_r =1. The dynamic response speed is faster than that in Fig. 12 (c) and is comparable with that in Fig. 11 (c).

0885-8993 (c) 2020 IEEE. Personal use is permitted, but republication/redistribution requires IEEE permission. See http://www.ieee.org/publications_standards/publications/rights/index.html for more information.
Authorized licensed use limited to: Aalborg Universitetsbibliotek. Downloaded on August 17,2020 at 06:26:16 UTC from IEEE Xplore. Restrictions apply.

This article has been accepted for publication in a future issue of this journal, but has not been fully edited. Content may change prior to final publication. Citation information: DOI 10.1109/TPEL.2020.3014365, IEEE Transactions on Power Electronics

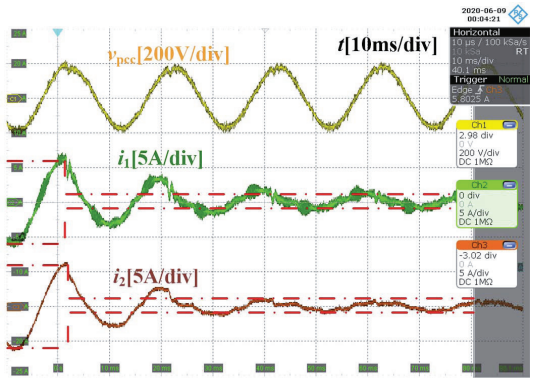

Fig. 15. Dynamic experimental waveforms of the step change of reference current (6A to 1A) for the grid-side current control when m = 4 and K_r = 1.

C. Tests in Capacitive-Impedance Grid Scenario

The Bode plots of the inverter output admittance and capacitive grid admittance for L_g = 9 mH (0.11 p.u.) and C_p = 22 μF (5.58 p.u.) are shown in Fig. 16, when m = 4 and K_r = 1 for RC. As shown in Fig. 16, for both inverter-side and grid-side current control, the inverter output admittance intersects with grid admittance in the non-passive region, so the PM is negative the system is unstable.

Fig. 17 (a) and (b) show the experimental waveforms when K_r = 1 and m changes from 2 to 4 for RC, viz., the inverter output admittance changes from all frequencies passive to partially non-passive and the inverter enters instability from stability. It can be seen from Fig. 17 (b) that the dominant oscillation component is around the intersection frequency, i.e., 1 kHz. Fig. 17 (c) gives dynamic experimental waveforms when K_r = 1 and m = 2 for RC, in which the dynamic response speed is also comparable with that in Fig. 11 (c). Fig. 18 (a) shows the experimental waveforms when m = 4 and K_r changes from 0.3 to 1 for RC, viz., in which the inverter output admittance changes from all frequencies passive to partially non-passive and the inverter enters instability from stability. The dominant oscillation amplified component is at the intersection frequency, i.e., 2.5 kHz. Fig. 18 (c) gives dynamic experimental waveforms when K_r = 0.3 and m = 4 for RC, in which the dynamic response speed is relatively slow and comparable with that in Fig. 12 (c).

D. Current Quality Evaluation in Distorted Grid Voltage Scenario

In order to show the superiority of the RC in harmonics rejection, tests are carried out in the presence of distorted grid voltage. In this experiment, the grid inductance is 9 mH (0.11 p.u.) and the distorted grid voltage is generated by connecting a three-phase rectifier to PCC.

As shown in Fig. 19 (a), when disabling RC, both the reference current tracking error (reference current is 6A) and the output current distortion are severe. However, after enabling RC, they are improved sharply. For the inverter-side current control, the inverter-side current is controlled to be sinusoidal with total harmonic distortion (THD) as low as

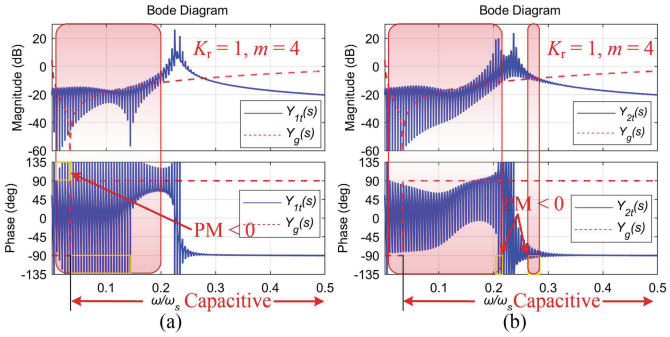

Fig. 16. Bode plots of $Y_{it}(s)$ and $Y_g(s)$ with m = 4, K_r = 1 for RC and L_g = 9 mH (0.11 p.u.), C_p = 22 μF (5.58 p.u.) for the grid. (a) Inverter-side current control. (b) Grid-side current control.

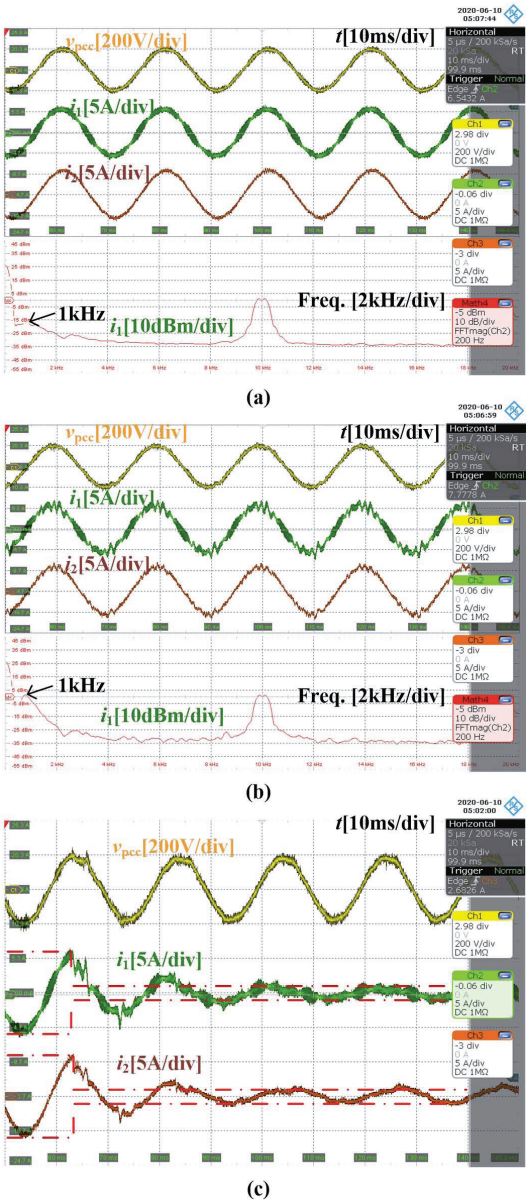

Fig. 17. Experimental waveforms of the inverter-side current control when K_r = 1 and m changes from (a) 2 to (b) 4. (c) Step change of reference current (6A to 1A, m = 2).

0885-8993 (c) 2020 IEEE. Personal use is permitted, but republication/redistribution requires IEEE permission. See http://www.ieee.org/publications_standards/publications/rights/index.html for more information.
Authorized licensed use limited to: Aalborg Universitetsbibliotek. Downloaded on August 17,2020 at 06:26:16 UTC from IEEE Xplore. Restrictions apply.

This article has been accepted for publication in a future issue of this journal, but has not been fully edited. Content may change prior to final publication. Citation information: DOI 10.1109/TPEL.2020.3014365, IEEE Transactions on Power Electronics

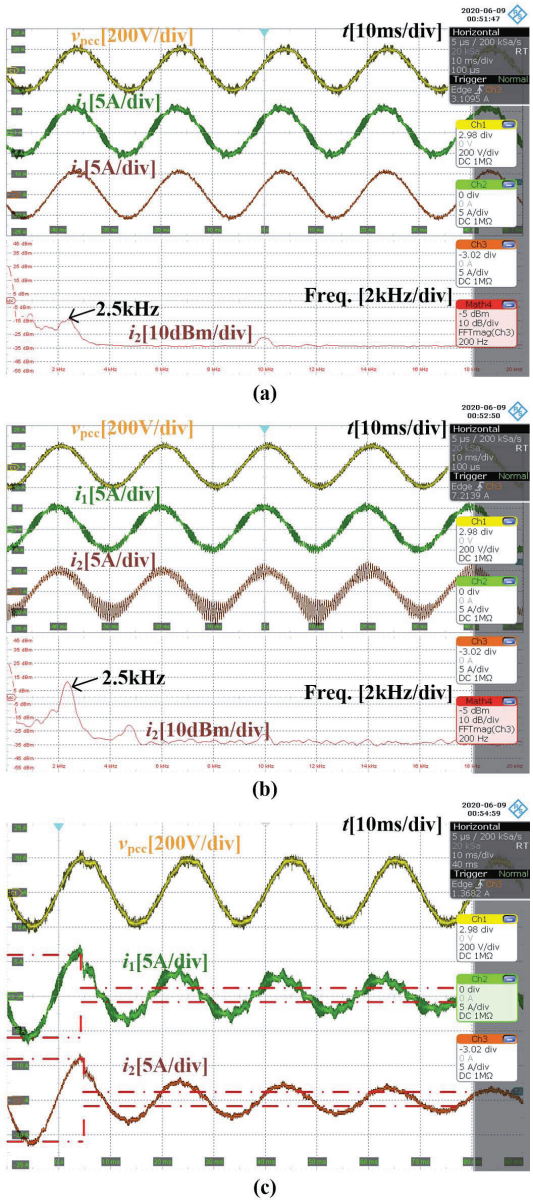

Fig. 18. Experimental waveforms of the grid-side current control when m = 4 and K_r changes from (a) 0.3 to (b) 1. (c) Step change of reference current (6A to 1A, K_r = 0.3).

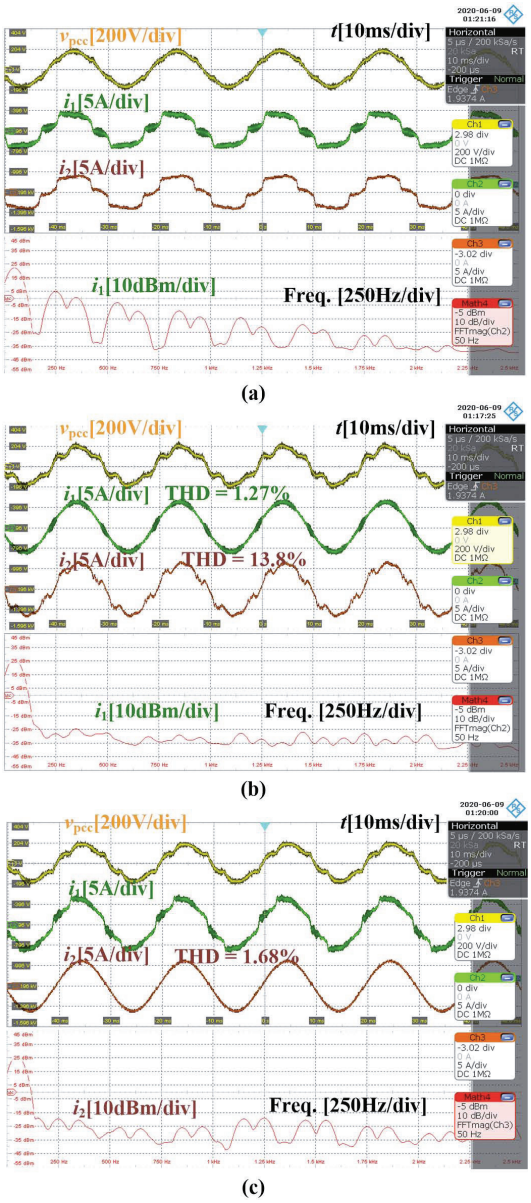

Fig. 19. Experimental waveforms in steady-state in the presence of distorted grid voltage. (a) Inverter-side current control without RC. (b) Inverter-side current control with RC. (c) Grid-side current control with RC.

1.27%, as shown in Fig. 19 (b). However, the grid injected current, viz., the grid-side current, is still highly distorted with THD as high as 13.8% since it is indirectly controlled and grid current harmonics can freely flow into the filter capacitor [36]. By contrast, for the grid-side current control, the grid-side current is directly controlled to be sinusoidal, as shown in Fig. 19 (c), and the THD of the current is reduced to 1.68%, which complies with the IEC standard (less than 5%). The experimental results of the harmonic rejection performance agrees well with the theoretical expectation in Fig. 9.

V. Conclusion

This paper presents an original passivity-based design method for RC for either inverter-side or grid-side current control of LCL-type inverters. Main contributions and the advantages of the proposed method are summarized as follows:

1) A general admittance model for either inverter-side or grid-side current-controlled LCL-type inverter, seen from the filter capacitor voltage, is built to facilitate the passivity-based stability assessment and controller parameter optimization. A unified analytical parameter selection method is applicable since the inner loop is a first-order system. Time-consuming iterations are thus avoided.
2) With the proposed method, all frequencies' passive output admittance is achieved for either inverter-side or grid-side current control embedded with RC. Therefore, the inverter can be connected to a grid regardless of the grid impedance (either inductive or capacitive), which means a robust plug-and-play functionality suitable for microgrid applications.

0885-8993 (c) 2020 IEEE. Personal use is permitted, but republication/redistribution requires IEEE permission. See http://www.ieee.org/publications_standards/publications/rights/index.html for more information.
Authorized licensed use limited to: Aalborg Universitetsbibliotek. Downloaded on August 17,2020 at 06:26:16 UTC from IEEE Xplore. Restrictions apply.

This article has been accepted for publication in a future issue of this journal, but has not been fully edited. Content may change prior to final publication. Citation information: DOI 10.1109/TPEL.2020.3014365, IEEE Transactions on Power Electronics

3) Thanks to the embedded RC, both the reference current tracking accuracy and the quality of the grid injected current can be improved even in the presence of distorted grid conditions. For the grid-side current control, the THD of the grid injected current can be reduced below 5%, which well complies with the IEC standard. However, the standard hasn't been fulfilled for the inverter-side current control since the grid injected current is indirectly controlled and current harmonics can freely flow into the filter capacitor [36]. Thus some special compensation schemes may be required to further improve the quality of the injected current, which would be the future work.

REFERENCES

[1] F. Blaabjerg, Zhe Chen, and S. B. Kjaer, "Power electronics as efficient interface in dispersed power generation systems," *IEEE Trans. Power Electron.*, vol. 19, no. 5, pp. 1184–1194, Sep. 2004.

[2] IEC, "Electromagnetic compatibility (EMC) - part 3-4: Limits - limitation of emission of harmonic currents in low-voltage power supply systems for equipment with rated current greater than 16 A."

[3] J. Dannehl, C. Wessels, and F. Fuchs, "Limitations of Voltage-Oriented PI Current Control of Grid-Connected PWM Rectifiers With LCL Filters," *IEEE Trans. Ind. Electron.*, vol. 56, no. 2, pp. 380–388, Feb. 2009.

[4] F. D. Freijedo, A. Vidal, A. G. Yepes, J. M. Guerrero, O. Lopez, J. Malvar, and J. Doval-Gandoy, "Tuning of Synchronous-Frame PI Current Controllers in Grid-Connected Converters Operating at a Low Sampling Rate by MIMO Root Locus," *IEEE Trans. Ind. Electron.*, vol. 62, no. 8, pp. 5006–5017, Aug. 2015.

[5] D. Zmood and D. Holmes, "Stationary Frame Current Regulation of PWM Inverters with Zero Steady-State Error," *IEEE Trans. Power Electron.*, vol. 18, no. 3, pp. 814–822, May. 2003.

[6] C. Xie, X. Zhao, K. Li, J. Zou, and J. M. Guerrero, "A New Tuning Method of Multiresonant Current Controllers for Grid-Connected Voltage Source Converters," *IEEE J. Emerg. Sel. Top. Power Electron.*, vol. 7, no. 1, pp. 458–466, Mar. 2019.

[7] C. Xie, X. Zhao, K. Li, J. Zou, and J. M. Guerrero, "Multirate Resonant Controllers for Grid-Connected Inverters With Harmonic Compensation Function," *IEEE Trans. Ind. Electron.*, vol. 66, no. 11, pp. 8981–8991, Nov. 2019.

[8] K. Zhou and D. Wang, "Digital Repetitive Controlled Three-Phase PWM Rectifier," *IEEE Trans. Power Electron.*, vol. 18, no. 1, pp. 309–316, Jan. 2003.

[9] A. Garcia-Cerrada, O. Pinzon-Ardila, V. Feliu-Batlle, P. Roncero-Sanchez, and P. Garcia-Gonzalez, "Application of a Repetitive Controller for a Three-Phase Active Power Filter," *IEEE Trans. Power Electron.*, vol. 22, no. 1, pp. 237–246, Jan. 2007.

[10] Z. Zou, K. Zhou, Z. Wang, and M. Cheng, "Frequency-Adaptive Fractional-Order Repetitive Control of Shunt Active Power Filters," *IEEE Trans. Ind. Electron.*, vol. 62, no. 3, pp. 1659–1668, Mar. 2015.

[11] C. Xie, X. Zhao, M. Savaghebi, L. Meng, J. M. Guerrero, and J. C. Vasquez, "Multirate Fractional-Order Repetitive Control of Shunt Active Power Filter Suitable for Microgrid Applications," *IEEE J. Emerg. Sel. Top. Power Electron.*, vol. 5, no. 2, pp. 809–819, Jun. 2017.

[12] K. Zhang, Y. Kang, J. Xiong, and J. Chen, "Direct repetitive control of SPWM inverter for UPS purpose," *IEEE Trans. Power Electron.*, vol. 18, no. 3, pp. 784–792, May. 2003.

[13] B. Zhang, D. Wang, K. Zhou, and Y. Wang, "Linear Phase Lead Compensation Repetitive Control of a CVCF PWM Inverter," *IEEE Trans. Ind. Electron.*, vol. 55, no. 4, pp. 1595–1602, Apr. 2008.

[14] G. Escobar, A. A. Valdez, J. Leyva-Ramos, and P. Mattavelli, "Repetitive-Based Controller for a UPS Inverter to Compensate Unbalance and Harmonic Distortion," *IEEE Trans. Ind. Electron.*, vol. 54, no. 1, pp. 504–510, Feb. 2007.

[15] S. Jiang, D. Cao, Y. Li, J. Liu, and F. Z. Peng, "Low-THD, Fast-Transient, and Cost-Effective Synchronous-Frame Repetitive Controller for Three-Phase UPS Inverters," *IEEE Trans. Power Electron.*, vol. 27, no. 6, pp. 2994–3005, Jun. 2012.

[16] Y. Wu and Y. Ye, "Internal Model-Based Disturbance Observer With Application to CVCF PWM Inverter," *IEEE Trans. Ind. Electron.*, vol. 65, no. 7, pp. 5743–5753, Jul. 2018.

[17] Y. Yang, K. Zhou, H. Wang, F. Blaabjerg, D. Wang, and B. Zhang, "Frequency Adaptive Selective Harmonic Control for Grid-Connected Inverters," *IEEE Trans. Power Electron.*, vol. 30, no. 7, pp. 3912–3924, Jul. 2015.

[18] Q. Zhao and Y. Ye, "A PIMR-Type Repetitive Control for a Grid-Tied Inverter: Structure, Analysis, and Design," *IEEE Trans. Power Electron.*, vol. 33, no. 3, pp. 2730–2739, Mar. 2018.

[19] P. Schülting, C. H. v. d. Broeck, and R. W. D. Doncker, "Analysis and Design of Repetitive Controllers for Applications in Distorted Distribution Grids," *IEEE Trans. Power Electron.*, vol. 34, no. 1, pp. 996–1004, Jan. 2019.

[20] W. Lu, K. Zhou, D. Wang, and M. Cheng, "A General Parallel Structure Repetitive Control Scheme for Multiphase DC-AC PWM Converters," *IEEE Trans. Power Electron.*, vol. 28, no. 8, pp. 3980–3987, Aug. 2013.

[21] T. Liu, D. Wang, and K. Zhou, "High-Performance Grid Simulator Using Parallel Structure Fractional Repetitive Control," *IEEE Trans. Power Electron.*, vol. 31, no. 3, pp. 2669–2679, 2016.

[22] L. Harnefors, R. Finger, X. Wang, H. Bai, and F. Blaabjerg, "VSC Input-Admittance Modeling and Analysis Above the Nyquist Frequency for Passivity-Based Stability Assessment," *IEEE Trans. Ind. Electron.*, vol. 64, no. 8, pp. 6362–6370, Aug. 2017.

[23] X. Wang, F. Blaabjerg, and P. C. Loh, "Passivity-Based Stability Analysis and Damping Injection for Multi-Paralleled Voltage-Source Converters with LCL Filters," *IEEE Trans. Power Electron.*, vol. PP, no. 99, pp. 1–1, 2017.

[24] L. Harnefors, A. Yepes, A. Vidal, and J. Doval-Gandoy, "Passivity-Based Controller Design of Grid-Connected VSCs for Prevention of Electrical Resonance Instability," *IEEE Trans. Ind. Electron.*, vol. 62, no. 2, pp. 702–710, Feb. 2015.

[25] R. D. Middlebrook, "Input filter consideration in design and application of switching regulators," *IEEE Industry Applications Soc. Arm. Meeting*, pp. 366–382, Jan. 1976.

[26] J. Sun, "Impedance-Based Stability Criterion for Grid-Connected Inverters," *IEEE Trans. Power Electron.*, vol. 26, no. 11, pp. 3075–3078, Nov. 2011.

[27] S. Vesti, T. Suntio, J. A. Oliver, R. Prieto, and J. A. Cobos, "Impedance-Based Stability and Transient-Performance Assessment Applying Maximum Peak Criteria," *IEEE Trans. Power Electron.*, vol. 28, no. 5, pp. 2099–2104, May. 2013.

[28] B. Wen, R. Burgos, D. Boroyevich, P. Mattavelli, and Z. Shen, "AC Stability Analysis and dq Frame Impedance Specifications in Power-Electronics-Based Distributed Power Systems," *IEEE J. Emerg. Sel. Top. Power Electron.*, vol. 5, no. 4, pp. 1455–1465, Dec. 2017.

[29] L. Harnefors, X. Wang, A. Yepes, and F. Blaabjerg, "Passivity-Based Stability Assessment of Grid-Connected VSCs: An Overview," *IEEE J. Emerg. Sel. Top. Power Electron.*, vol. 4, no. 1, pp. 116–125, Mar. 2016.

[30] L. Harnefors, L. Zhang, and M. Bongiorno, "Frequency-domain passivity-based current controller design," *IET Power Electronics*, vol. 1, no. 4, pp. 455–465, Dec. 2008.

[31] A. Akhavan, H. R. Mohammadi, J. C. Vasquez, and J. M. Guerrero, "Passivity-Based Design of Plug-and-Play Current-Controlled Grid-Connected Inverters," *IEEE Trans. Power Electron.*, vol. 35, no. 2, pp. 2135–2150, Feb. 2020.

[32] C. Xie, K. Li, J. Zou, D. Liu, and J. M. Guerrero, "Passivity-Based Design of Grid-Side Current-Controlled LCL-Type Grid-Connected Inverters," *IEEE Trans. Power Electron.*, vol. 35, no. 9, pp. 9813 – 9823, 2020.

[33] C. Xie, K. Li, J. Zou, and J. M. Guerrero, "Passivity-Based Stabilization of LCL-Type Grid-Connected Inverters via a General Admittance Model," *IEEE Trans. Power Electron.*, vol. 35, no. 6, pp. 6636–6648, Jun. 2020.

[34] L. Harnefors, A. G. Yepes, A. Vidal, and J. Doval-Gandoy, "Passivity-Based Stabilization of Resonant Current Controllers With Consideration of Time Delay," *IEEE Trans. Power Electron.*, vol. 29, no. 12, pp. 6260–6263, Dec. 2014.

[35] E. Wu and P. W. Lehn, "Digital Current Control of a Voltage Source Converter With Active Damping of LCL Resonance," *IEEE Trans. Power Electron.*, vol. 21, no. 5, pp. 1364–1373, Sep. 2006.

[36] Z. Xin, P. Mattavelli, W. Yao, Y. Yang, F. Blaabjerg, and P. C. Loh, "Mitigation of Grid-Current Distortion for LCL-Filtered Voltage-Source Inverter With Inverter-Current Feedback Control," *IEEE Trans. Power Electron.*, vol. 33, no. 7, pp. 6248–6261, Jul. 2018.

0885-8993 (c) 2020 IEEE. Personal use is permitted, but republication/redistribution requires IEEE permission. See http://www.ieee.org/publications_standards/publications/rights/index.html for more information.
Authorized licensed use limited to: Aalborg Universitetsbibliotek. Downloaded on August 17,2020 at 06:26:16 UTC from IEEE Xplore. Restrictions apply.

This article has been accepted for publication in a future issue of this journal, but has not been fully edited. Content may change prior to final publication. Citation information: DOI 10.1109/TPEL.2020.3014365, IEEE Transactions on Power Electronics

Chuan Xie (Senior Member, IEEE) received the B.S. degree in automation engineering from the University of Electronic Science and Technology of China (UESTC), Chengdu, China, and the Ph.D. degree in power electronics from Zhejiang University (ZJU), Hangzhou, China, in 2007 and 2012, respectively.

Since 2012, he was a Lecturer with the School of Automation Engineering at UESTC, where he was promoted as an Associate Professor in 2019. From May 2015 to May 2016, he was a Visiting Scholar at the Department of Energy Technology, Aalborg University (AAU). His main research interests include digital control of power electronics, grid synchronization technology, distributed generation systems, microgrids and power quality.

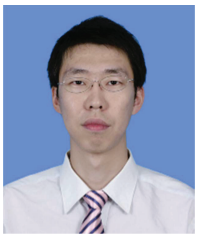

Dong Liu (Senior Member, IEEE) received the B.Eng. and M.Sc. in electrical engineering from South China University of Technology, Guangzhou, China, in 2008 and 2011, and the Ph.D. degree in energy technology from the Department of Energy Technology, Aalborg University, Aalborg, Denmark, in 2018. Currently, he is with the Department of Energy Technology in Aalborg University as a Postdoctoral Researcher.

From 2011 to 2014, he was an R&D engineer in Emerson Network Power Co., Ltd., Shenzhen, China. From May, 2017 to November, 2017, he was a visiting scholar at Center for Power Electronics Systems (CPES), Virginia Tech, Blacksburg, VA, USA. His main research interests include the modeling and control of power electronics converters, high efficiency power conversion systems, and power electronics applications in renewable energy power generations.

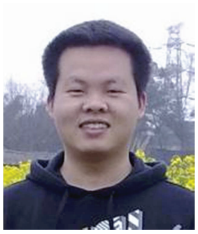

Kai Li (Member, IEEE) received the B.S., M.S., and Ph.D. in Automation Engineering from the University of Electronic Science and Technology of China, Chengdu, China in 2006, 2009, and 2014, respectively.

From 2009 to 2016, he was an Assistant Professor with the School of Automation Engineering, University of Electronic Science and Technology of China, Chengdu, China. From 2016.2 to 2017.2, he was an Guest Researcher with the Department of Energy Technology, Aalborg University, Denmark. Since 2016, he has been an Associate Professor with the School of Automation Engineering, University of Electronic Science and Technology of China, Chengdu, China. His research interests include multilevel inverters, storage converters, and microgrids.

Jianxiao Zou (Member, IEEE) received the B.S., M.S., and Ph.D. degrees in control science and engineering from the University of Electronic Science and Technology of China, Chengdu, China in 2000, 2003, and 2009, respectively.

He is currently a professor at University of Electronic Science and Technology of China (UESTC). He served as Vice Dean of School of Automation Engineering from 2011. He also served as the vice president of Sichuan Electrotechnical Society, vice president of Society for electrical engineering, and the Chairman of member development, Chengdu Section of IEEE China. He was a visiting scholar of University of California, Berkeley (UC Berkeley) in 2010 and senior visiting professor of Rutgers, The State University of New Jersey in 2014. He organized more than 10 international conferences/symposiums as general/program chairs and Session Chair. He has been publishing more than 50 journal papers and has been authorized more than 120 national invention patents. His research interests include control theory and control engineering, renewable energy control technologies, intelligent information processing and control.

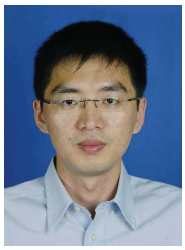

Keliang Zhou (Senior Member, IEEE) received the B.Sc. degree from the Huazhong University of Science and Technology, Wuhan, China, in 1992, the M.Eng. degree from the Wuhan University of Technology, Wuhan, in 1995, and the Ph.D. degree in electrical engineering from Nanyang Technological University, Singapore, in, 2002, respectively. Since 2014, he has been a Senior Lecturer with the School of Engineering, University of Glasgow, Glasgow, U.K. He has authored or co-authored one monograph, Periodic Control of Power Electronic Converters, and more than 100 technical papers. He holds several granted patents in relevant areas.

His current research interests include power electronics and electric drives, renewable energy generation, control theory and applications, and microgrid technology.

Josep M. Guerrero (Fellow, IEEE) received the B.S. degree in telecommunications engineering, the M.S. degree in electronics engineering, and the Ph.D. degree in power electronics from the Technical University of Catalonia, Barcelona, in 1997, 2000 and 2003, respectively. Since 2011, he has been a Full Professor with the Department of Energy Technology, Aalborg University, Denmark, where he is responsible for the Microgrid Research Program. From 2012 he is a guest Professor at the Chinese Academy of Science and the Nanjing University of Aeronautics and Astronautics; from 2014 he is chair Professor in Shandong University; and from 2015 he is a distinguished guest Professor in Hunan University.

His research interests is oriented to different microgrid aspects, including power electronics, distributed energy-storage systems, hierarchical and cooperative control, energy management systems, and optimization of microgrids and islanded minigrids.

0885-8993 (c) 2020 IEEE. Personal use is permitted, but republication/redistribution requires IEEE permission. See http://www.ieee.org/publications_standards/publications/rights/index.html for more information.
Authorized licensed use limited to: Aalborg Universitetsbibliotek. Downloaded on August 17,2020 at 06:26:16 UTC from IEEE Xplore. Restrictions apply.